

ON THE STABILITY OF LOW-MASS PLANETS WITH SUPERCRITICAL HYDROSPHERES

H. G. VIVIEN,^{1,2} A. AGUICHINE,¹ O. MOUSIS,¹ M. DELEUIL,¹ AND E. MARCQ³

¹*Aix Marseille Univ, CNRS, CNES, LAM, Marseille, France*

²*Laboratoire de Physique et Chimie de l'Environnement et de l'Espace (LPC2E), UMR CNRS 7328 - Université d'Orléans, Orléans, France*

³*LATMOS/IPSL, UVSQ Université Paris-Saclay, Sorbonne Université, CNRS, Guyancourt, France*

(Received ; Revised ; Accepted)

Submitted to The Astrophysical Journal

ABSTRACT

Short-period and low-mass water-rich planets are subject to strong irradiation from their host star, resulting in hydrospheres in supercritical state. In this context, we explore the role of irradiation on small terrestrial planets that are moderately wet in the low-mass regime ($0.2\text{--}1M_{\oplus}$). We investigate their bulk properties for water contents in the 0.01–5% range by making use of an internal structure model that is coupled to an atmosphere model. This coupling allows us to take into account both the compression of the interior due to the weight of the hydrosphere and the possibility of atmospheric instability in the low-mass regime. We show that even for low masses and low water contents, these planets display inflated atmospheres. For extremely low planetary masses and high irradiation temperatures, we find that steam atmospheres become gravitationally unstable when the ratio η of their scale height to planetary radius exceeds a critical value of ~ 0.1 . This result is supported by observational data, as all currently detected exoplanets exhibit values of η smaller than 0.013. Depending on their water content, our results show that highly irradiated and low-mass planets up to $0.9M_{\oplus}$ with significative hydrospheres are not in stable form and should lose their volatile envelope.

Keywords: planets and satellites: composition, planets and satellites: ocean, planets and satellites: atmospheres, planets and satellites: detection

arXiv:2204.07451v1 [astro-ph.EP] 15 Apr 2022

1. INTRODUCTION

Earth-like mass planets represent the ultimate goal of exoplanets detection (Kaltenegger & Faherty 2021). With today’s facilities, their observed number is ever increasing, requiring efforts to enable their characterization, that is accurate measurement of their mass and radius. Due to their small orbital periods, many of those planets are highly irradiated by their parent stars, implying the needs to develop dedicated interior and atmosphere models to investigate their structure and evolution (Mousis et al. 2020; Acuña et al. 2021; Aguichine et al. 2021). In addition, better understanding of the evolution of the hydrosphere of such planets is key to investigate their potential habitability conditions.

In this study, we investigate the bulk properties of highly irradiated low-mass planets in the $0.2\text{--}1M_{\oplus}$ range, and with water contents varying between 0.01% and 5%. These water contents values roughly bracket the water mass fraction (WMF) estimated for the Earth and Jupiter’s moon Europa, respectively.

This mass range is also close to the one found by dynamical simulations investigating the formation of water-rich and habitable planets (Raymond et al. 2007). These mass and water content ranges have not been properly quantified so far in the literature because conventional models (e.g. Zeng et al. 2016, 2019; Turet et al. 2019) describe the internal structures of planets with thick atmospheres neglecting the combination of two important effects: i) the compression of the interior due to the weight of the hydrosphere, and ii) the possibility of atmospheric instability at low planetary masses. While the latter can be overlooked for temperate planets, it is critical for high irradiation temperatures and sub-Earth masses. To overcome this issue, we use a self-consistent model in which the atmosphere is coupled with the interior.

2. MODEL

2.1. Upgrades

The model used here is built upon the one described in Aguichine et al. (2021), and includes two major improvements. First, the grid from which the atmospheric properties are interpolated has been extended to surface gravities as low as 1 m.s^{-2} , coupled with a revised convergence scheme. In the new convergence scheme, the atmosphere’s properties are updated only when the interior model has stabilized. This revision greatly reduces the occurrence of numerical instability in extreme cases, when planetary mass and radius’ values are close to the boundaries of the considered range, ensuring convergence to the solution. Second, the atmosphere model now includes a module which assesses the hydrostatic

stability of water-rich atmospheres at given planetary mass. This new and improved version expands the operational validity range towards lower masses and smaller WMFs. The model now allows the computation of atmospheres for planets with gravities (g_b), masses, and boundary temperatures in the ranges $1 \leq g_b \leq 30 \text{ m.s}^{-2}$, $0.2 \leq M_p \leq 20M_{\oplus}$, and $750 \leq T_b \leq 4500 \text{ K}$.

2.2. Principle

Our model assumes a planet composed of differentiated layers with various compositions including an iron-dominated core, a lower mantle, an upper mantle and a fluid (from solid to near-plasma) water layer (Mousis et al. 2020; Aguichine et al. 2021). The top of the hydrosphere is a water-dominated atmosphere that follows the prescriptions of Marcq et al. (2017, 2019) and Pluriel et al. (2019). The structure of the planets assumes hydrostatic equilibrium and adiabatic heat transfer, and takes into account radiative transfer in the atmosphere to generate its physical properties. By doing so, our model self-consistently takes into account the compression of the internal layers of the planet which results from the presence of a hydrosphere.

Three parameters set the distribution of all chemical species in the different layers of the interior model: the fraction of alloy in the core f_{alloy} , the overall Mg/Si ratio of the planet, and the amount of iron present in the silicate mantle $\text{Mg}\# = \left(\frac{\text{Mg}}{\text{Mg}+\text{Fe}} \right)_{\text{Mantle}}$, which describes the level of differentiation of the planet. Two required compositional inputs of the model are the planet’s core mass fraction (CMF) and WMF. Pressure and temperature profiles are integrated from the outside, and require the inputs of the boundary pressure P_b and the boundary temperature T_b . Finally, the model also requires the input of the planet’s mass M_b (subscript b denotes the mass encapsulated within the boundary of the interior model, and excludes the atmospheric contribution).

Once defined, the input parameters allow for the computation of the planet’s internal structure and associated boundary radius. The atmosphere model provides the Outgoing Longwave Radiation (OLR), albedo, thickness and mass of the atmosphere as a function of the bulk mass and radius, and T_b . The atmospheric vertical profile is assumed adiabatic until the temperature drops to the skin temperature $T_0 = T_{\text{eff}}/2^{1/4}$, and isothermal above (Marcq et al. 2017, 2019). We choose $P_{\text{tr}} = 20 \text{ mbar}$ as the pressure of the transiting radius, which corresponds to the altitude where the opacity of the atmosphere is close to unity. Summing the atmosphere’s mass and thickness with the bulk ones yields the final mass M_p and radius R_p of the planet, respectively. The mass of the water present in the atmosphere is computed

by integrating its density profile, and is taken into account in the total water content of the planet. While the mass of the atmosphere is typically much smaller than the planet itself ($\sim 0.01\%$), this correction is crucial for planets with low water mass fractions.

The interior and atmosphere modules are connected at a given boundary pressure $P_b = 300$ bar, which corresponds to the transition between the vapor and supercritical phases. This threshold is computed for each planet, and thus provides us with an accurate determination of the surface pressure P_{surf} exerted on the refractory layers. Similarly, the temperature at the bottom of the atmosphere T_b is computed iteratively for an input irradiation temperature T_{irr} , leading to a true surface temperature T_{surf} .

2.3. Stability criterion

To determine the minimum mass at which a water atmosphere remains stable, we fix a criterion derived from analytical considerations. Modeling the atmosphere beyond P_{tr} as a simple theoretical extended isothermal atmosphere¹ of temperature T_{irr} , the pressure at infinity would be expressed as (Catling & Kasting 2017):

$$P_{\infty} = P_{\text{tr}} \exp\left(-\frac{GM_p m}{kT_{\text{irr}} R_p}\right), \quad (1)$$

where G is the gravitational constant, k is the Boltzmann constant, and m is the mass of the molecule composing the atmosphere (here H_2O). This pressure is small but finite, and must correspond to the particle density in the interplanetary medium (IPM), namely $n_{\text{IPM}} = \frac{P_{\text{IPM}}}{kT_{\text{irr}}}$, for the atmosphere to be gravitationally bounded. If the value of P_{∞} is smaller than P_{IPM} , then the atmosphere contracts in order to reach the expected IPM pressure, and stabilizes. In the opposite situation, the atmosphere escapes from the planet via the Parker wind mechanism (Wang & Dai 2018). Combining the inequality $P_{\infty} > P_{\text{IPM}}$ with Eq. 1, we derive a criterion for an atmosphere to be unstable:

$$H > \eta R_p, \quad (2)$$

where $H = \frac{kT_{\text{irr}} R_p^2}{GM_p m}$ is the planet's height scale, and $\eta = \left(\ln \frac{P_{\text{tr}}}{P_{\text{IPM}}}\right)^{-1}$ is a dimensionless parameter. If H/R_p is larger than η , the atmosphere is considered hydrostatically unstable. Because the atmosphere loses its mass by Parker wind in a finite timescale, the value of

η in Eq. 2 is in fact underestimated. However computing the timescale of atmospheric loss would require a level of modeling that is beyond the scope of this paper. Instead, we estimate η from the output of our model, which can then be used as a conservative estimate of the stability likelihood of a planet.

2.4. Investigated ranges

In this study, the compositional parameters f_{alloy} , Mg/Si, and Mg# of the different mineral layers are assumed to be equal to 0.13, 1.131, and 0.9, respectively. These values correspond to those derived for the Earth (Sotin et al. 2007; Brugger et al. 2017; Aguichine et al. 2021). To determine the impact of the water content on both the mass-radius relationships and the internal structure of low-mass planets, the WMF of our interior model has been set to three different values, namely, 0.01%, 1%, and 5%.

The irradiation temperature T_{irr} is explored in the 500–2000 K range, which essentially covers the domain of irradiation temperatures of exoplanets discovered so far. Because a change in the core mass fraction is expected to impact both the planet's surface gravity and atmospheric structure, three CMF values have been chosen in our simulations, namely, 0, 0.325, and 0.7. These CMF values correspond to the cases of rocky planets, Earth-like planets (Sotin et al. 2007), and Mercury-like planets (Stacey 2005; Benz et al. 2007), respectively. Our computation grid follows a logarithmic mass distribution in the $0.2\text{--}1.0M_{\oplus}$ range and linear between $1.0\text{--}2.3M_{\oplus}$, but only planets possessing hydrostatically stable atmospheres are shown. This mass range was previously unavailable as the model from Aguichine et al. (2021) could hardly compute the structure of planets of masses below $0.5 M_{\oplus}$. Note that the minimum mass of $0.2M_{\oplus}$ has been chosen because it roughly corresponds to the smallest detectable mass today (see Figure. 1 of Deleuil et al. (2020)).

3. RESULTS

Figure 1 shows the planetary radii (scaled in Earth radii) as a function of planetary mass and irradiation temperature. This radius corresponds to the altitude where the pressure reaches $P_{\text{tr}} = 20$ mbar in the hydrosphere. Each column corresponds to CMF values of 0, 0.325 and 0.7, respectively. Each row corresponds to WMF of 0.01%, 1% and 5%, respectively. The different panels of the figure cover a mass range where the atmosphere is in hydrostatic equilibrium. In each panel, the upper left corner exhibit a boundary between hydrostatically stable and unstable planets, which depends on the adopted CMF and WMF. Panels with smaller CMF and

¹ Gravity variation is taken into account.

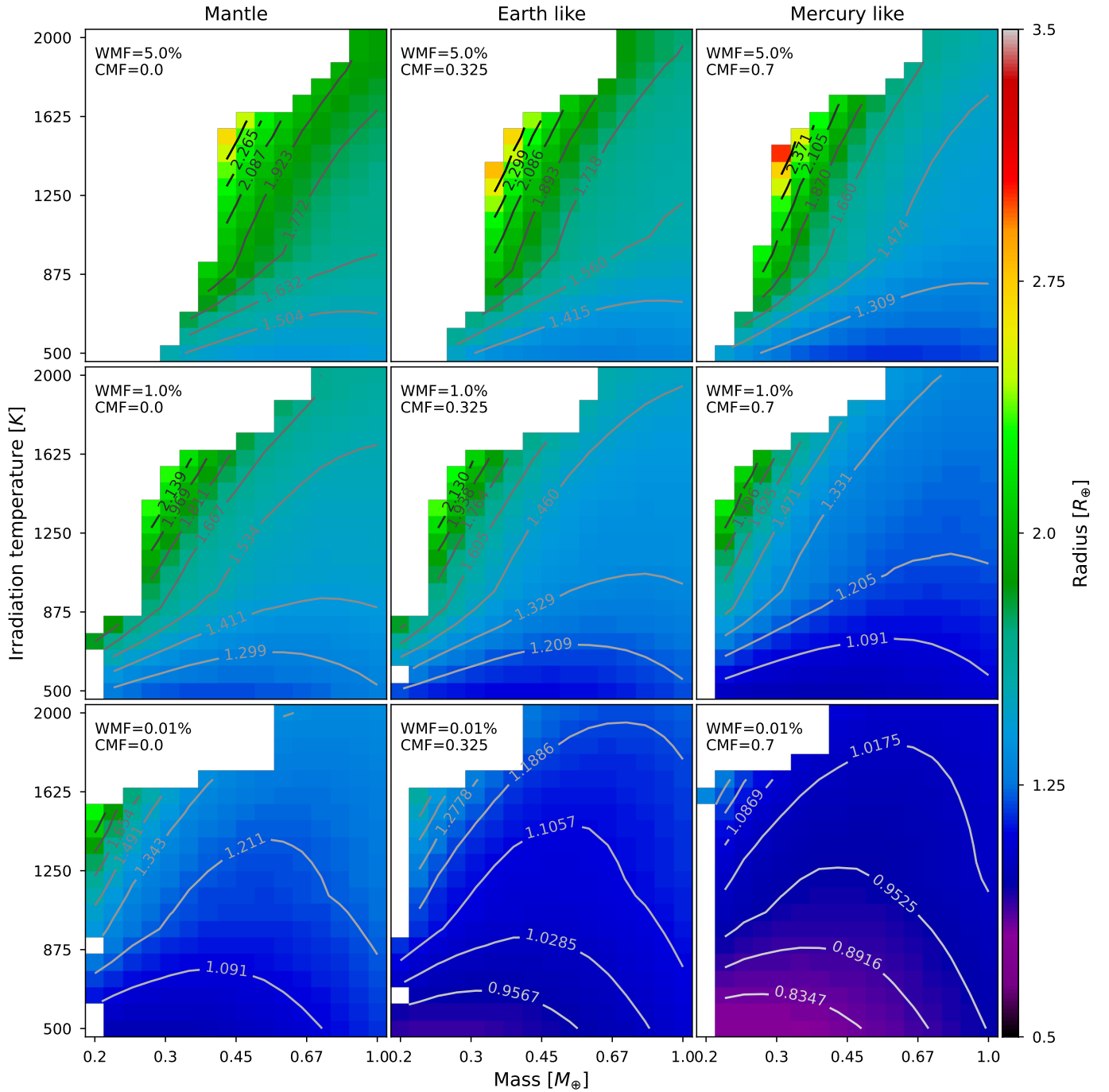


Figure 1. Computed planetary radii R_p at the transiting depth $P_{tr} = 20\text{mbar}$ as a function of planetary mass M_p and irradiation temperature T_{irr} . Contours show lines of constant planetary radii (in units of Earth radius) to improve the readability of each panel. Left, center and right columns correspond to CMF values that represent pure mantle (0.0), Earth-like (0.325) and Mercury-like (0.7), respectively. Top, middle and bottom rows correspond to WMFs of 5%, 1% and 0.01%, respectively. The missing data correspond to cases excluded from our calculations, due to hydrostatic instability.

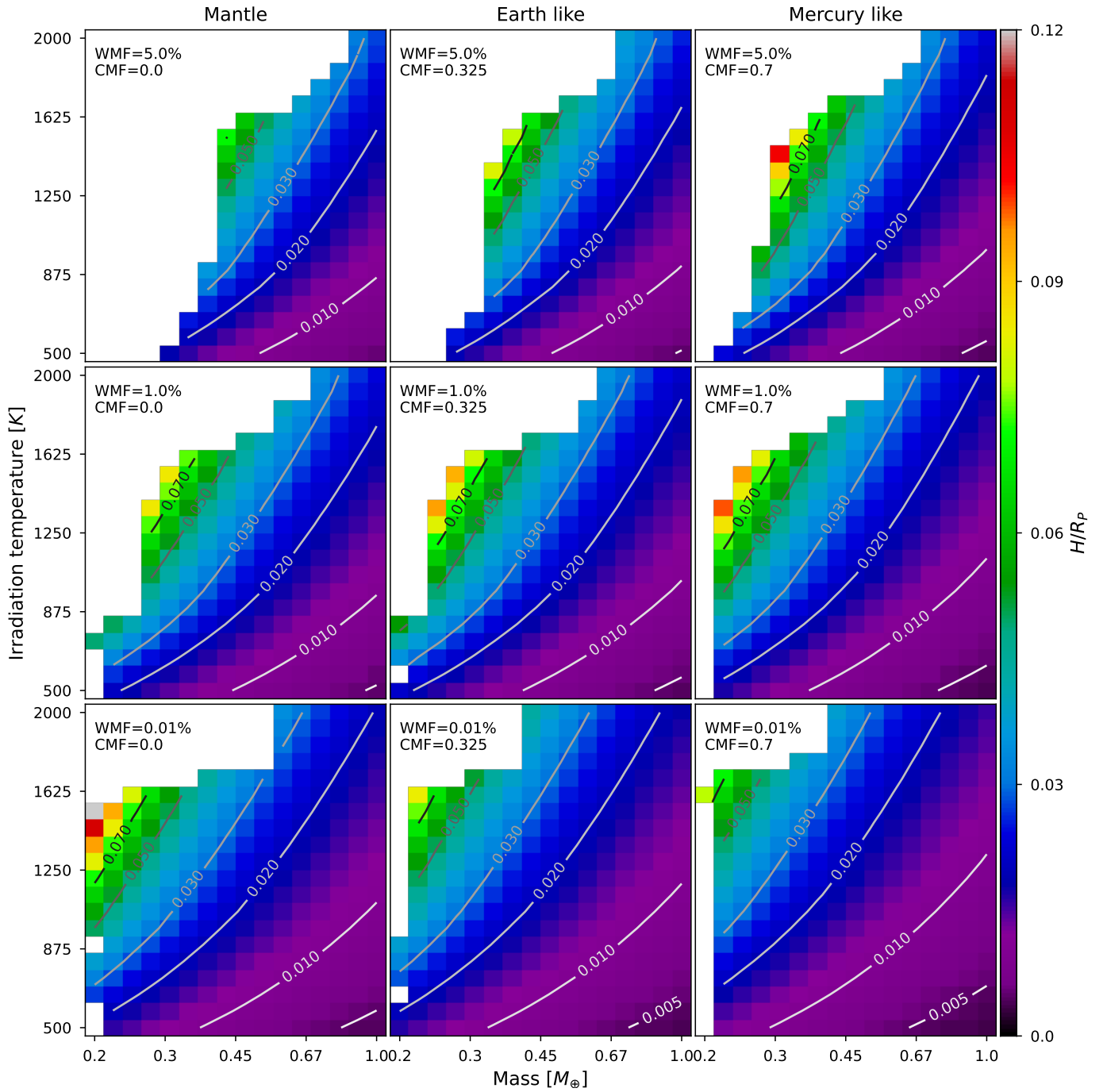


Figure 2. Similar to Figure 1, but with a color scheme representing the H/R_p contours.

higher WMF, which result in lower bulk densities, have more planets with unstable hydrospheres.

In most cases, the planetary radius increases with irradiation temperature and decreases with planetary mass, as an effect of the competition between thermal energy and gravitational binding. This also indicates that the planetary radius is dominated by the atmosphere’s thickness. For planets with low water content (i.e. bottom panels of Figure 1 showing WMF = 0.01%), the radius increases with mass when $M_p \sim 0.5M_\oplus$. This indicates a regime where the planetary radius is less sensitive to the atmosphere’s thickness. Sharp corners in the boundary between stable and unstable planets (e.g. top panels at $T_{\text{irr}} \simeq 1500$ K and $M_p \simeq 0.3 M_\oplus$, or middle row at $T_{\text{irr}} \simeq 1400$ K and $M_p \simeq 0.25 M_\oplus$) are visual artefacts caused by the finite resolution of the grid from which atmospheric properties are interpolated. With an infinite precision, more points would be available between these corners. Therefore, this edge corresponds to cases that are the closest to the physical boundary between stable and unstable atmospheres.

Figure 2 shows the H/R_p ratio as a function of planetary mass and irradiation temperature. Contours of constant H/R_p values seem parallel to the boundary between stable and unstable atmospheres. The highest computed values of H/R_p indicate that η is $\simeq 0.1$ for our model, and has no apparent correlation with the CMF or the WMF. This value is almost $\sim 3\text{--}4$ times higher than the theoretical estimate ($\eta = 0.026\text{--}0.035$) found for $T_{\text{irr}} = 500\text{--}2000$ K, $P_{\text{tr}} = 10^{-3}\text{--}20$ mbar, and $n_{\text{IPM}} = 5 \times 10^6 \text{ m}^{-3}$ (Catling & Kasting 2017). In the currently confirmed population of exoplanets², assuming pure H₂O atmospheres, we find that the H/R_p ratio is mainly in the $10^{-3}\text{--}10^{-2}$ range for planets with masses smaller than $2.3 M_\oplus$. Using Kepler-51 b’s planetary parameters derived by Masuda (2014), we also find that this planet exhibits one of the highest H/R_p ratio ($0.013^{+0.006}_{-0.010}$), which is consistent with the aforementioned $10^{-3}\text{--}10^{-2}$ range. Even if the assumption of a pure steam atmosphere is likely to be unrealistic, this computation gives an upper bound to the criterion. This value is most certainly an observational limitation, better detection capabilities will allow to constrain more precisely the boundary between stable and unstable atmospheres based on the H/R_p criterion.

A similar criterion was derived by Owen & Wu (2016) for planets with a pure H/He envelope, based on the ratio between the planet’s radius and its Bondi radius ($R_p/R_B = 2H/R_p$). Interestingly, the authors also find

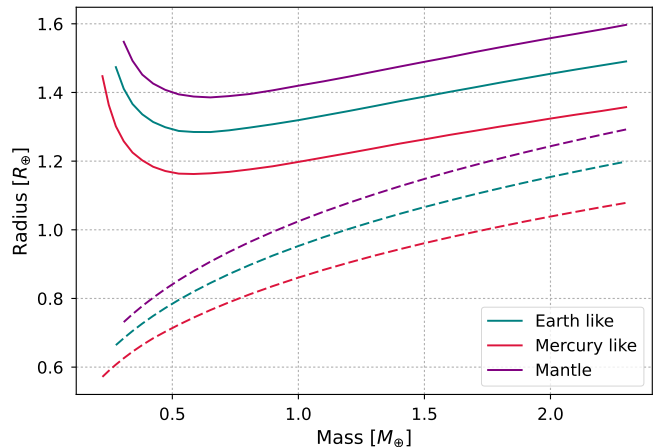


Figure 3. Mass-radius relationships calculated for three CMFs, WMF = 5% and $T_{\text{irr}} = 500$ K. Dotted and solid lines correspond to the base and the top of the hydrosphere, respectively.

that the atmosphere is lost over a short timescale when this ratio exceeds 0.1. In addition, Fossati et al. (2017) did a similar study using the restricted Jeans escape parameter $\Lambda = R_p/H$ for H/He-rich planets and found that the atmosphere becomes unstable under a value estimated to be $\sim 15\text{--}35$ (equivalent to the previous criterion $R_p = 0.1R_B$). Planets with Λ values as low as 10 ($H/R_p \gtrsim 0.1$) are present in our panels. Cubillos et al. (2017) achieved a similar result and concluded that for the few low-mass planets that exhibit Λ values as low as 10, it is likely that either their mass is underestimated or their radius is overestimated. For this latter case, the possible presence of aerosols in the atmosphere would increase its opacity, and lead to an overestimated transit radius (Wang & Dai 2019; Gao & Zhang 2020; Ohno & Tanaka 2021).

Figure 3 shows mass-radius profiles extracted from Figure 1, and calculated in the cases of three CMF values, assuming WMF = 5% and $T_{\text{irr}} = 500$ K. This figure illustrates the fact that an increase of the CMF increases the surface gravity, and as a consequence reduces the size of the hydrosphere at fixed planetary mass. Even in the case of moderately wet planets (WMF $\sim 5\%$), the pressure at the bottom of the hydrosphere can easily reach the GPa range. The subsequent compression of the interior is no longer negligible, and leads to an increase of the surface gravity. This induces thinner atmospheres, for which the blanketing effect is more moderate.

To illustrate the implications of the H/R_p boundary criterion, we estimate the maximum WMF as a function of planetary mass and temperature. For each value of M_p and T_{irr} we fit the planetary radius as a function of the WMF with a power-law function to derive a simple relationship between R_p and the WMF. We

² <http://exoplanet.eu/>

then set $H/R_p = 0.1$, and compute the maximal radius using $H = \frac{kT_{\text{irr}}R_p^2}{GM_p m}$. Finally, we invert the fitted radius-to-WMF relation to compute the theoretical maximum WMF that can be achieved. Results are presented in Figure 4, and show that the stability criterion of the atmosphere strongly limits the amount of H_2O that can be present in low-mass planets.

To quantify the feedback of the hydrosphere on the interior and the resulting radius, Figure 5 compares our results to those obtained by Turbet et al. (2020). These authors used a pre-defined interior model from Zeng et al. (2016) coupled with their own atmospheric model. In this comparison, T_{irr} is set to 500K, and corresponds to 10.38 times the solar insolation received by the Earth. The mass-radius relationships from Zeng et al. (2016) are computed at a surface pressure of 1 bar, and become inappropriate for the modeling of wet planets, since the bottom of the hydrosphere can reach up to 10 GPa. This leads to the contraction of the refractory interior of up to 4% with a WMF of 5%. In turn, this contraction induces a slight increase of the surface gravity that reduces the atmosphere’s thickness. The two effects add up to produce a difference in planetary radii of up to $\sim 10\%$. For negligible water contents, both models yield similar results.

When comparing the hydrospheres alone, our model exhibits thinner hydrospheres than the model of Turbet et al. (2020) in most cases. An additional cause of this could be the use of the steam tables from Haar et al. (1984), which meet several limitations. The corresponding data points can be safely extrapolated up to 3 GPa and 2500 K, but the pressure and temperature at the bottom of the hydrosphere are mostly above this limit (up to $\sim 4500\text{K}$ and 10 GPa). As a result, the adiabatic gradient cannot be extrapolated precisely, leading to an isothermal profile. Under those conditions, the density is overestimated, meaning that the radius is underestimated. In our model, we also use the steam tables from Haar et al. (1984) to compute the atmosphere’s structure. However, we switch to the equation of state from Mazevet et al. (2019) at $P_b = 300$ bar (supercritical layer). Thanks to this, all equations of state remain in their respective domains of validity within the investigated temperature and pressure ranges. However, given the complexity of both models, it is difficult to list all sources of deviation and precisely quantify their effect. This also highlights the necessity of using identical and up-to-date equations of state when comparing the outcomes of interior models elaborated by different groups.

4. CONCLUSION

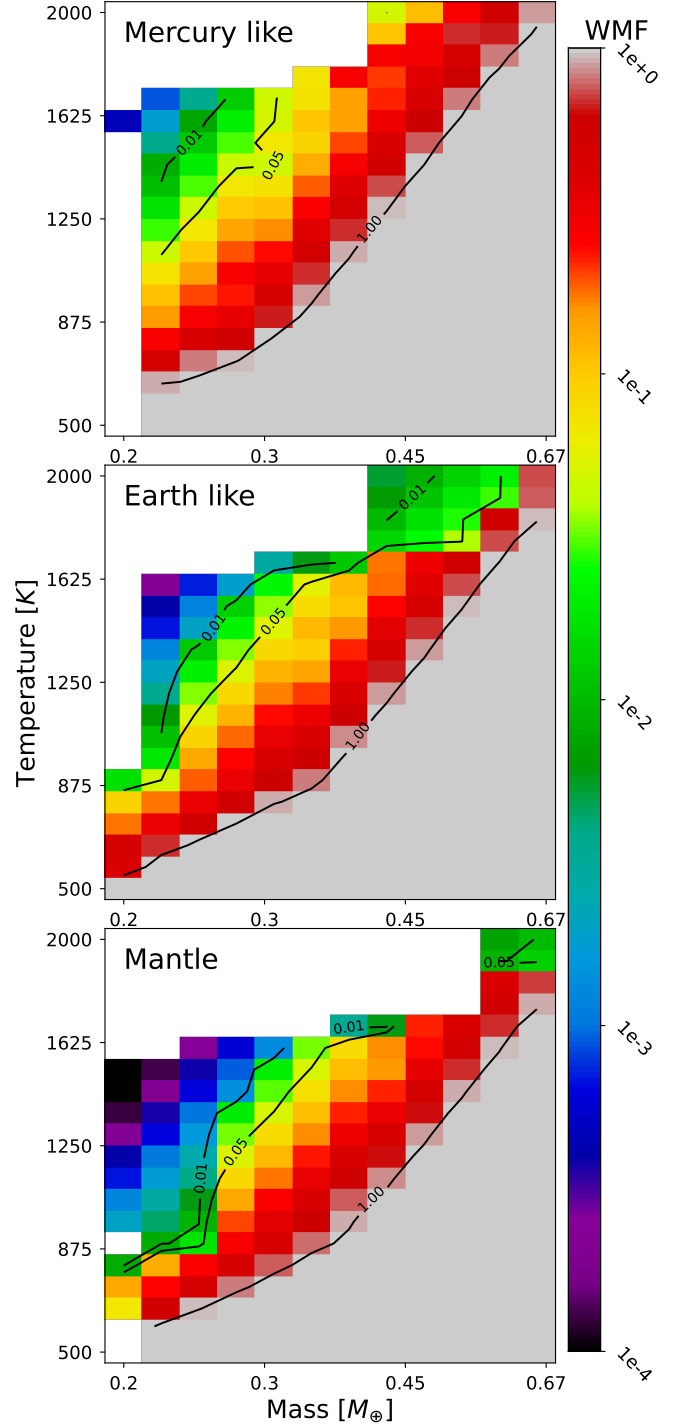


Figure 4. Maximum WMF as a function of planetary mass and irradiation temperature predicted by our model for CMF values representing mantle-like, Earth-like and Mercury-like interiors. All WMF are calculated assuming $H/R_p = 0.1$, and using a power law fitted to our results. Contours represent different values of WMF. For example, the grey region corresponds to planets fully made of water.

We have explored the role of irradiation on small terrestrial planets that are moderately wet in the low-mass regime ($0.2\text{--}2.3M_{\oplus}$). To that purpose, we have investigated their bulk properties for water contents varying between 0.01% and 5% using an upgraded interior and atmospheric structure model based on the one described in [Aguichine et al. \(2021\)](#). The upgrade of this model includes i) an extension of the grid of atmospheric properties to gravities down to 1 m.s^{-2} , and ii) the assessment of the hydrostatic stability of water-rich atmospheres at given planetary mass. This coupling allows us to take into account both the compression of the interior due to the weight of the hydrosphere and the possibility of instability of the water layer in the low-mass regime.

Our results show that the compression of the interior should indeed be taken into account to derive proper planetary structure. In the investigated $0.2\text{--}2.3M_{\oplus}$ mass range, the pressure is found to be in the 0.03–10 GPa range at the bottom of the hydrosphere, depending on the adopted WMF. This causes the refractory part to contract by up to $\sim 4\%$ in the explored parameter range. The uncompressed case would correspond to a typical Earth-like atmosphere with a 1-bar pressure at its bottom. Despite this compression, even for low masses and low water contents, the irradiation causes these planets to display inflated atmospheres and increased planetary radius. We also find that the combination of low planetary masses and high irradiation temperatures in-

duce gravitationally unstable steam atmospheres. These planets are subject to fast atmospheric loss when their H/R_p ratio exceeds $\simeq 0.1$. This value is consistent with the H/R_p ratios found in the population of detected exoplanets, which are mostly smaller than 0.01. We finally point out that, according to our model, some planets with H/R_p ratios suggesting rapidly escaping H/He atmospheres could in fact be water-dominated planets ([Cubillos et al. 2017](#); [Wang & Dai 2019](#); [Gao & Zhang 2020](#); [Ohno & Tanaka 2021](#)).

Interestingly, the mass limit below which the atmosphere is unstable in our simulations could shift toward larger masses if thermal escape is considered. Given the high irradiation temperatures, thermal escape can lead to a complete loss of the whole hydrosphere ([Lopez & Fortney 2013](#); [Owen & Wu 2013](#); [Kurosaki et al. 2014](#); [Lopez 2017](#); [Aguichine et al. 2021](#)). This supports the idea that highly irradiated and low-mass planets with thick hydrospheres should not be common, as they lack gravitationally stable atmospheres.

5. ACKNOWLEDGEMENTS

O.M. and M.D. acknowledge support from CNES. The project leading to this publication has received funding from the Excellence Initiative of Aix-Marseille Université - A*Midex, a French “Investissements d’Avenir programme” AMX-21-IET-018. We also extend our thanks to the anonymous referee for their insight and useful comments.

REFERENCES

- Acuña, L., Deleuil, M., Mousis, O., et al. 2021, *A&A*, 647, A53. doi:10.1051/0004-6361/202039885
- Aguichine, A., Mousis, O., Deleuil, M., et al. 2021, *ApJ*, 914, 84. doi:10.3847/1538-4357/abfa99
- Benneke, B., Wong, I., Piaulet, C., et al. 2019b, *ApJL*, 887, L14 doi:10.3847/2041-8213/ab59dc
- Benz, W., Anic, A., Horner, J., et al. 2007, *SSRv*, 132, 189. doi:10.1007/s11214-007-9284-1
- Brugger, B., Mousis, O., Deleuil, M., et al. 2017, *ApJ*, 850, 93. doi:10.3847/1538-4357/aa965a
- Catling, D. C. & Kasting, J. F. 2017, *Atmospheric Evolution on Inhabited and Lifeless Worlds*, by David C. Catling, James F. Kasting, Cambridge, UK: Cambridge University Press, 2017
- Cubillos, P., Erkaev, V., Juvan, I., et al. 2017, *MNRAS*, 466, 1868. doi:10.1093/mnras/stw3103
- Deleuil, M., Pollacco, D., Baruteau, C., et al. 2020, *SSRv*, 216, 105. doi:10.1007/s11214-020-00726-2
- Fossati, L., Erkaev, N. V., Lammer, H., et al. 2017, *A&A*, 598, A90. doi:10.1051/0004-6361/201629716
- Gao, P. & Zhang, X. 2020, *ApJ*, 890, 93. doi:10.3847/1538-4357/ab6a9b
- Grasset, O., Castillo-Rogez, J., Guillot, T., et al. 2017, *SSRv*, 212, 835. doi:10.1007/s11214-017-0407-z
- Haar, L., Gallagher, J. S., & Kell, G. S., *NBS/NRC steam tables thermodynamic and transport properties and computer programs for vapor and liquid states of water in SI units*. (Washington DC: Hemisphere Publication Corporation).
- Kaltenegger, L. & Faherty, J. K. 2021, *Nature*, 594, 505. doi:10.1038/s41586-021-03596-y
- Kurosaki, K., Ikoma, M., & Hori, Y. 2014, *A&A*, 562, A80. doi:10.1051/0004-6361/201322258
- Léger, A., Selsis, F., Sotin, C., et al. 2004, *Icarus*, 169, 499. doi:10.1016/j.icarus.2004.01.001
- Lopez, E. D. & Fortney, J. J. 2013, *ApJ*, 776, 2. doi:10.1088/0004-637X/776/1/2

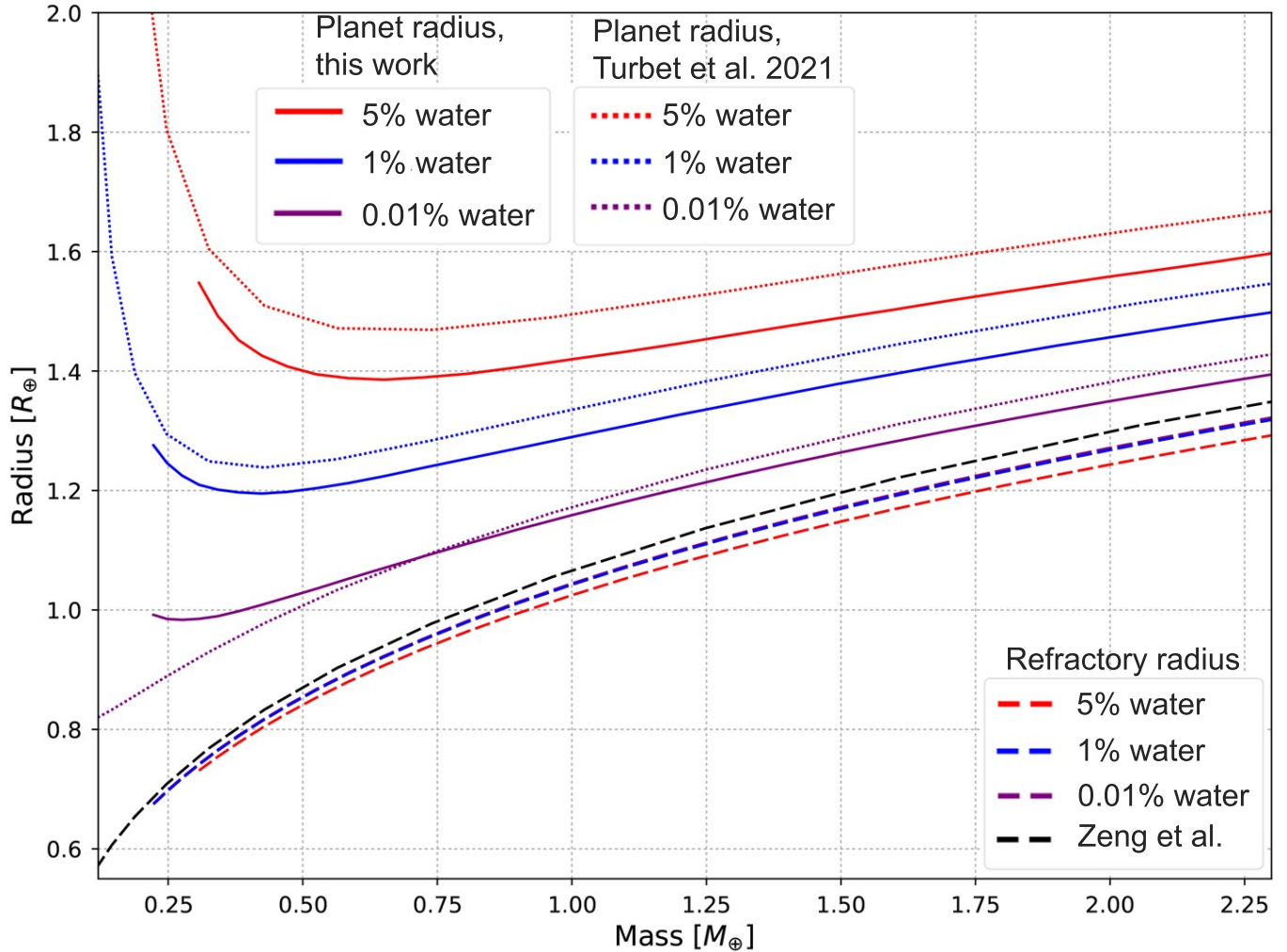


Figure 5. Comparison between the mass-radius relationships computed from our model (red, blue, and purple solid lines) and that of Turbet et al. (2020) (red, blue, and purple dotted lines) for $T_{\text{irr}} = 500\text{K}$ and $\text{CMF} = 0$. Both models define the transiting radius as the altitude where the opacity is close to unity. The colored and black dashed lines correspond to the base of the hydrosphere computed from our approach and that of Turbet et al. (2020), respectively.

Lopez, E. D. 2017, MNRAS, 472, 245.

doi:10.1093/mnras/stx1558

MacDonald, R. J., & Madhusudhan, N. 2019, MNRAS, 486, 1292 doi:10.1093/mnras/stz789

Marcq, E., Salvador, A., Massol, H., et al. 2017, Journal of Geophysical Research (Planets), 122, 1539.

doi:10.1002/2016JE005224

Marcq, E., Baggio, L., Lefèvre, F., et al. 2019, Icarus, 319, 491. doi:10.1016/j.icarus.2018.10.006

Masuda, K. 2014, ApJ, 783, 53.

doi:10.1088/0004-637X/783/1/53

Mazevet, S., Musella, R., & Guyot, F. 2019, A&A, 631, L4. doi:10.1051/0004-6361/201936288

Mousis, O., Deleuil, M., Agüichine, A., et al. 2020, ApJL, 896, L22. doi:10.3847/2041-8213/ab9530

Ohno, K. & Tanaka, Y. 2021, ApJ, 920, 124.

doi:10.3847/1538-4357/ac1516

Owen, J. E. & Wu, Y. 2013, ApJ, 775, 105.

doi:10.1088/0004-637X/775/2/105

Owen, J. E. & Wu, Y. 2016 ApJ, 717, 107.

doi:10.3847/0004-637X/817/2/107

Pluriel, W., Marcq, E., & Turbet, M. 2019, Icarus, 317, 583. doi:10.1016/j.icarus.2018.08.023

Raymond, S. N., Quinn, T., & Lunine, J. I. 2007, Astrobiology, 7, 66. doi:10.1089/ast.2006.06-0126

Russell, S. S., Ballentine, C. J., & Grady, M. M. 2017, Philosophical Transactions of the Royal Society of London Series A, 375, 20170108.

doi:10.1098/rsta.2017.0108

Sotin, C., Grasset, O., & Mocquet, A. 2007, Icarus, 191, 337. doi:10.1016/j.icarus.2007.04.006

- Stacey, F. D. 2005, *Reports on Progress in Physics*, 68, 341.
doi:10.1088/0034-4885/68/2/R03
- Turbet, M., Ehrenreich, D., Lovis, C., et al. 2019, *A&A*, 628, A12. doi:10.1051/0004-6361/201935585
- Turbet, M., Bolmont, E., Ehrenreich, D., et al. 2020, *A&A*, 638, A41. doi:10.1051/0004-6361/201937151
- Wang, L. & Dai, F. 2018, *ApJ*, 860, 175.
doi:10.3847/1538-4357/aac1c0
- Wang, L. & Dai, F. 2019, *ApJL*, 873, L1.
doi:10.3847/2041-8213/ab0653
- Zeng, L., Sasselov, D. D., & Jacobsen, S. B. 2016, *ApJ*, 819, 127. doi:10.3847/0004-637X/819/2/127
- Zeng, L., Jacobsen, S. B., Sasselov, D. D., et al. 2019, *Proceedings of the National Academy of Science*, 116, 9723. doi:10.1073/pnas.1812905116